Anatomy of black veins in Zagami: clues to the formation of high-pressure phases

Falko Langenhorst *, Jean-Paul Poirier [1]

Bayerisches Geoinstitut, Universität Bayreuth, D-95440 Bayreuth, Germany

Abstract

Black melt veins in the Martian basaltic meteorite Zagami were investigated using analytical transmission electron microscopy, with the goal to constrain the mechanisms and *PTt* conditions that result in the formation of high-pressure phases therein. Our study reveals the existence of a number of high-pressure minerals: stishovite, K- and Na,Ca-rich hollandites, akimotoite (silicate ilmenite), as well as amorphous grains of silicate perovskite composition. Crystals of a ferro-magnesian silicate titanite with a low Ca content have been identified for the first time. The veins formed by rapid shear melting and solidified in extremely short times. As a consequence, the vein melt could not homogeneously mix and it partially preserves the chemical heterogeneity of precursor minerals, accounting for the large diversity of high-pressure minerals. Most of the tiny phases directly crystallized from the melt under high pressure at very high temperatures. Silicate perovskite probably amorphized upon decompression and evolved, at its grain boundaries, by solid-state diffusion toward the lower pressure assemblage wüstite+stishovite. Not only do these observations help to understand the formation of high-pressure phases in shock events, but they also provide clues to the mineralogical complexity that can be expected in planetary mantles.   © 2000 Elsevier Science B.V. All rights reserved.

Keywords: Martian meteorites; impacts; high pressure; minerals; titanite; perovskite; cooling; diffusion

1. Introduction

The Zagami achondrite fell on October 3, 1962 in Nigeria (11°44′N, 7°5′E), with a total weight of 18 kg. It belongs to the group of basaltic shergot-

* Corresponding author. Tel.: +49-921-55-3727;
Fax: +49-921-55-3769;
E-mail: falko.langenhorst@uni-bayreuth.de

[1] Permanent address: Département des Géomatériaux, Institut de physique du globe de Paris, 4 place Jussieu, 75252 Paris Cedex 05, France.

tites: a subgroup of the SNC meteorites, which have probably been ejected from Mars by a bolide impact [1]. The strongest indication for a Martian origin of Zagami is given by atmospheric noble gases that were trapped in shock-produced melt pockets [2]. Zagami has a young crystallization age of 180 Ma; its impact age is about 3 Ma. The exact meaning of these ages is however still under discussion [1]. The mineralogy of Zagami is simple; the major phases are augite, pigeonite, and maskelynite (feldspar amorphized during shock) [3,4]. Irregular zoning and exsolution lamellae in clinopyroxenes record a two-stage magmatic history [3]. Initial crystallization of Mg-rich

pyroxene nuclei in a deep-seated magma was followed by overgrowth with Fe-rich rims, occurring in a lava flow or a near-surface dyke. Maskelynite, mosaicism in pyroxene, and pockets and veins of shock melt provide evidence for later shock metamorphism. The black shock veins, from 1 to 100 μm wide, are usually interpreted as resulting from shear melting during shock. They are fresh and well-preserved, which is due to the fortunate circumstance that Zagami is a fall. In a previous study [5], we could observe an unaltered high-pressure mineral assemblage consisting of stishovite, $KAlSi_3O_8$ hollandite, and K-bearing omphacite. These phases formed by crystallization from the shear-induced high-pressure melt.

We report here on the identification of a number of further high-pressure phases and comprehensive observations of the microtexture of the veins, using analytical transmission electron microscopy (ATEM) and electron diffraction. Together with calculated estimates of the times required for cooling and crystallization of the veins and solid-state diffusion in minerals, the ATEM observations allow us to propose a self-consistent scenario for the formation of the high-pressure phases.

2. Experimental

Polished thin sections were prepared from a 1.1 g sample of Zagami provided by R. Haag; 3 mm wide discs were cored from the thin sections containing the black veins and glued onto TEM copper grids. These specimens were then thinned to perforation by Ar ion beam bombardment at 3.5 keV and an incidence angle of 13°. For TEM investigation, we used a Philips FEG CM20 STEM equipped with a Noran Vantage energy-dispersive X-ray (EDX) analyzer. Imaging techniques employed to characterize the microtexture of the veins and the defects and exsolution phenomena in minerals were conventional (CTEM), scanning (STEM), and high-resolution (HRTEM) transmission electron microscopy. Mineral phases were identified on the basis of EDX microanalyses and selected area electron diffraction (SAED). To minimize electron beam damage of the sensitive

high-pressure minerals, we used a liquid nitrogen cooling stage. Quantification of the microanalyses involved an absorption correction procedure based on the principle of electroneutrality [6]. The oxygen k-line serves as a measure of sample thickness. $k_{x/Si}$ factors were determined according to the parameter-less correction method [7], using a set of silicate standards. A more detailed description of the quantification procedure is given in [8]. X-ray elemental distribution maps have been acquired in dynamical scanning mode using a drift compensation program.

3. TEM observations and analyses

TEM examination focused on the internal structure of the shock veins, the identification of minerals therein, and the deformation, transformation, and exsolution phenomena in adjacent minerals. In our thin sections of Zagami, the black veins have thicknesses varying from 1 up to 100 μm. The veins are clast-poor and usually follow grain boundaries but they sometimes cut through minerals. In the following, we will consider and compare two cases of vein configuration: (i) a 100 μm thick vein region with adjacent pyroxene and maskelynite and (ii) a 1 μm thin vein with pyroxene on both sides. These two cases of vein configuration are instructive examples for the complexity of veins in terms of microtexture, mineralogy, and cooling history.

3.1. Thick vein region with plagioclase contribution

In the first case, the adjacent plagioclase is completely converted to maskelynite; there are no crystalline relicts. Such relatively thick (100 μm) vein zones with a plagioclase contribution are fully crystallized at the margins and are mainly composed of omphacite, i.e. Na- and Al-bearing pyroxene (Fig. 1A). In the central part a glassy silicate groundmass is observed, containing polycrystalline aggregates or single crystals of high-pressure minerals (Fig. 1B). Here, K-rich hollandite and stishovite had previously been identified [5]. Further inspection also revealed the presence of Ca,Na-rich hollandite polycrystals, similar in
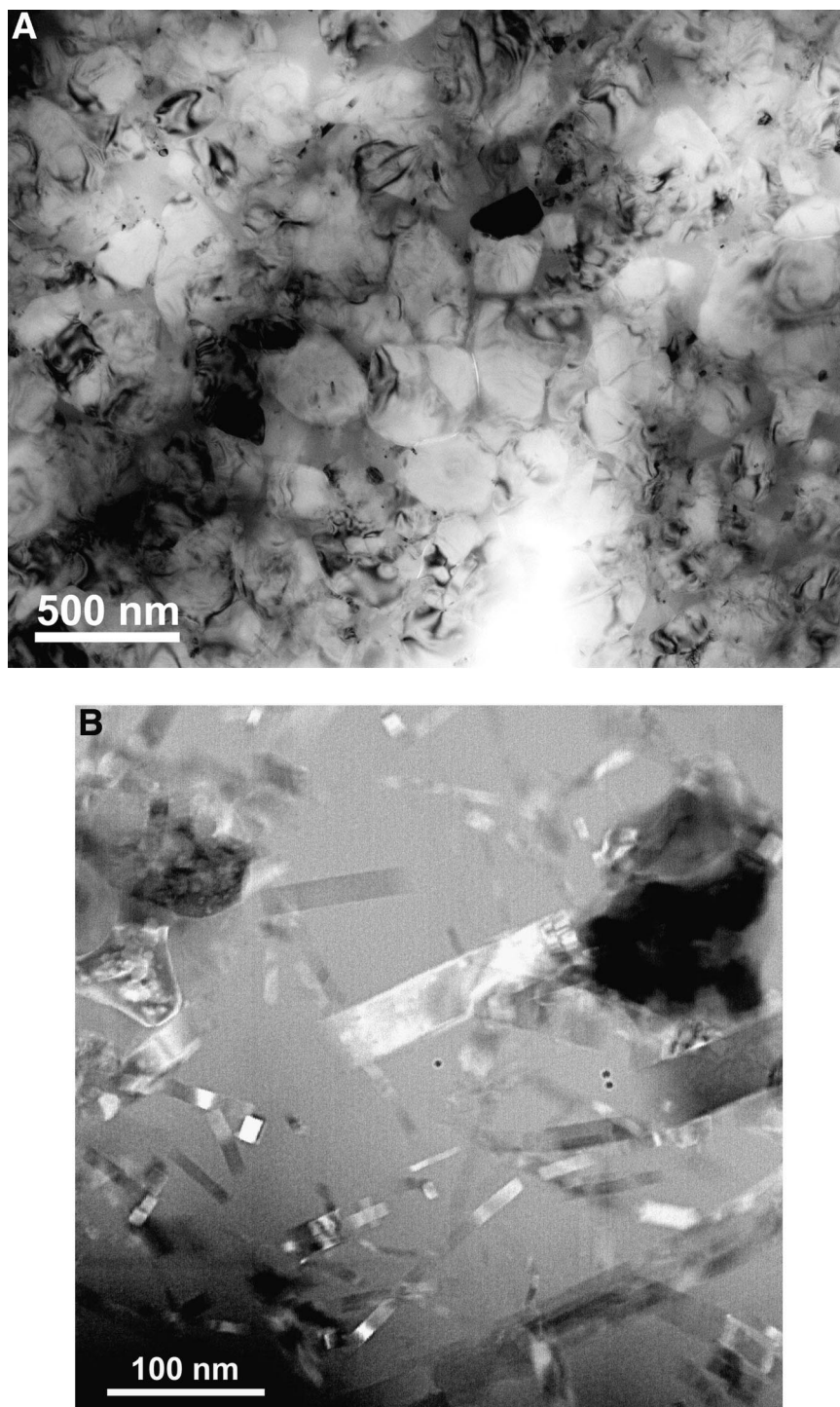
Fig. 1. (A) Bright field TEM image of the margin of a 100 μm thick vein, composed of numerous pyroxene grains. (B) Dark field STEM image showing numerous stishovite needles and few troilite grains embedded in a glassy silicate matrix. This microtexture is observed in the central parts of the 100 μm wide vein.

textural appearance to the previously discovered K-rich hollandite. These polycrystalline Na,Ca-rich aggregates are approximately 1 μm in diameter; the size of individual crystallites is of the order of 20–30 nm (Fig. 2). Considerable loss of Na and, to a lesser extent, of Ca occurs upon exposure to the electron beam, leading to an apparent non-stoichiometric formula $(Na_{0.33}Ca_{0.44})(Al_{1.39}Si_{2.62})O_8$ (Table 1). The Al/Si ratio indicates an 'An$_{56}$' content, compatible with the composition of maskelynite in the bulk meteorite [3,4]. This intermediate composition could indicate that there is a complete solid solution series between a Na- and Ca-pure endmember hollandite, similar to the low-pressure plagioclase series.

Six diffraction lines could be observed before the electron beam-sensitive hollandite aggregate completely transformed to the amorphous state. The indexing of electron diffraction patterns yields the following d-spacings consistent with the hollandite structure: 3.24 Å (220), 2.94 Å (310), 2.05 Å (420), 1.98 Å (301), 1.63 Å (440), and 1.32 Å (002). A refinement of these d-spacings yields the following lattice parameters: $a = 9.19(2)$ Å, $c = 2.63(1)$ Å, and $V = 222.3(1.3)$ Å^3. The lattice parameters of the Na,Ca-rich hollandite are smaller and, consequently, its density ($\rho = 4.07$ g/cm^3) is larger than those of the K-rich hollandite ($a = 9.39$ Å, $c = 2.76$ Å, $V = 242.9$ Å^3, $\rho = 3.84$ g/cm^3; [5]). This is in agreement with previous data [9,10] and the fact that the ionic radii of Na^+ and Ca^{2+} are smaller than that of K^+.

3.2. Thin vein region in pyroxene

Vein regions as thin as 1 μm occur where two pyroxenes have been sheared against each other or where a vein is crosscutting a single pyroxene.

Table 1
Representative EDX–TEM microanalyses of akimotoite, silicate titanite, (Na,Ca)-hollandite, and amorphous grains representing a break-down product of silicate 'perovskite'

	Akimotoite	Titanite	'Perovskite'	'Perovskite'	'Perovskite'	Hollandite
Weight percent						
Si	25.7	30.3	23.7	24.6	19.9	27.5
Ti	0.1	0.1	0.2	0.1	3.3	nd
Al	0.2	0.6	0.4	0.5	0.3	14.0
Cr	0.2	0.1	0.2	0.2	0.2	nd
Fe	15.5	13.6	15.5	16.9	29.5	0.7
Mn	0.1	0.4	0.2	0.3	0.3	nd
Mg	14.1	5.2	6.3	10.4	4.9	nd
Ca	0.5	5.0	12.4	4.8	3.3	6.5
Na	nd	nd	nd	nd	nd	2.8
K	nd	nd	nd	nd	nd	0.5
O	43.6	44.6	41.1	42.3	38.3	47.8
Number of cations						
Si	1.01	1.94	0.98	0.99	0.89	2.62
Al	0.01	0.04	0.02	0.02	0.02	1.39
Cr	< 0.01	< 0.01	< 0.01	< 0.01	< 0.01	nd
Ti	< 0.01	< 0.01	0.01	< 0.01	0.09	nd
Fe^{3+}	nd	nd	nd	nd	nd	0.03
Fe^{2+}	0.31	0.44	0.32	0.34	0.66	nd
Mg	0.64	0.38	0.30	0.49	0.25	nd
Mn	< 0.01	0.01	0.01	0.01	0.01	nd
Ca	0.01	0.23	0.36	0.14	0.10	0.44
Na	nd	nd	nd	nd	nd	0.33
K	nd	nd	nd	nd	nd	0.04
Σ cations	1.99	3.04	2.00	1.99	2.02	4.85
O	3	5	3	3	3	8

Quantification of spectra involved the calibration of k-factors and an absorption correction.
nd: not detected; relative errors are 1–2% (1σ) for major elements and one order of magnitude larger for trace elements.
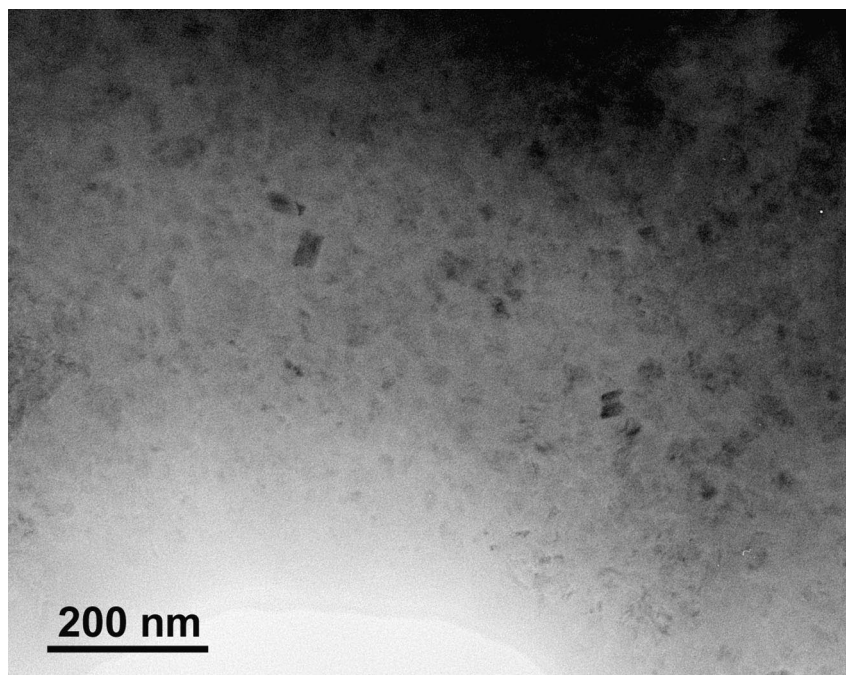
Fig. 2. Bright field TEM image of a polycrystalline Na,Ca-rich hollandite aggregate. The composition of this aggregate, which rapidly amorphized under the electron beam, is given in Table 1.
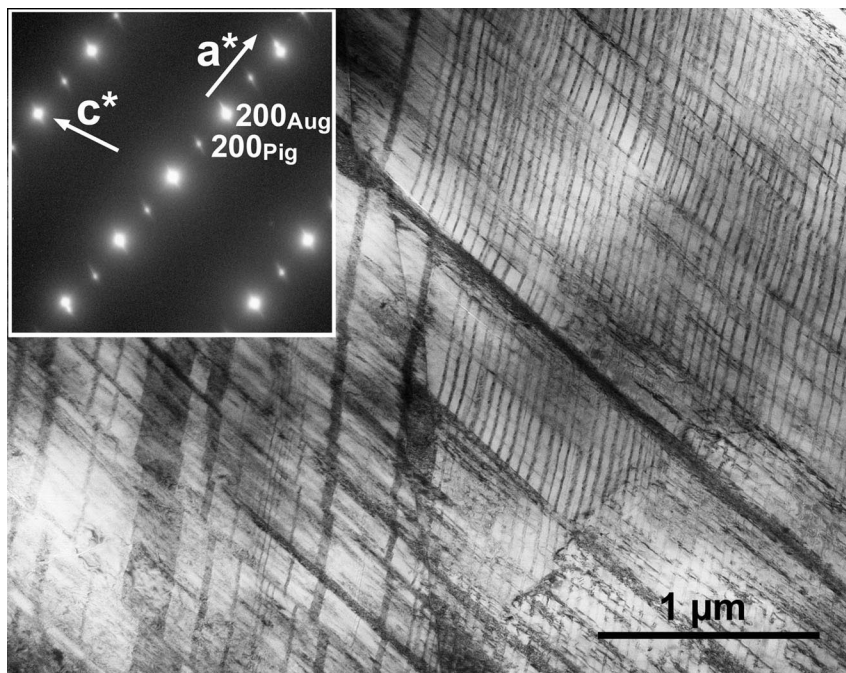

Fig. 3. Bright field TEM image of augite with numerous pigeonite exsolution lamellae parallel to the (001) plane. Note the offsetting of pigeonite lamellae, which is due to the activation of (100) glide bands. The inset shows the splitting of spots in the a* directions, revealing the different β angles of augite and pigeonite.
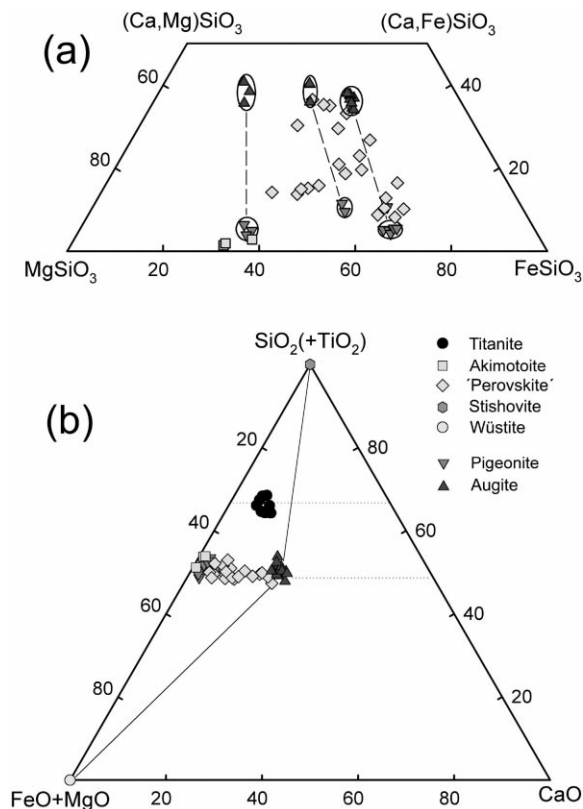
Fig. 4. Compositions of various phases occurring adjacent to or in a 1 μm thin vein plotted in (a) the pyroxene quadrilateral and (b) a ternary SiO_2–CaO–(MgO+FeO) diagram.

Detailed observations have been made in a region of a vein with two adjacent augite crystals. To understand and interpret the observations within the thin vein, it is necessary to first consider the subsolidus exsolution and deformation microstructures in adjacent pyroxenes. The exsolution phenomena reflect the cooling history of pyroxenes following crystallization in the magma chamber, whereas the deformation features record the mechanical response to the shock event.

The augite crystals contain numerous coherent pigeonite exsolution lamellae, parallel to the (001) planes of both the pigeonite and the augite host (Fig. 3). The complete crystallographic relationship between augite and pigeonite is: $b_{aug}//b_{pig}$ and $c_{aug}//c_{pig}$. In the zone axis pattern taken along the b^* axis, splitting of reflections is observed in the a^* directions (inset in Fig. 3), resulting from the different monoclinic angles β in pigeonite

(108.5°) and augite (106°). The pigeonite lamellae in Mg-rich cores are thicker and more widely spaced than those in the Fe-rich rims. Mean values for the thickness of and spacing between pigeonite lamellae are 68 and 96 nm in the core and 13 and 36 nm in the rim, respectively. A second set of even thinner pigeonite lamellae approximately parallel to (100) is also sometimes observed in augite rims. In comparison to Shergotty [11], the exsolution phenomena in Zagami occur at a finer scale, indicating a faster cooling rate. Using model data on the coarsening of exsolution lamellae in clinopyroxene [12], the wavelength of the pigeonite lamellae in Zagami record a cooling rate ≤1 K/h. The compositions of augite–pigeonite pairs adjacent to the vein have been measured at three different places along the vein and are plotted in Fig. 4a,b. The large compositional variations in Fe, Mg, and Ca contents reflect the observation that the vein is cutting through rim and core regions of augite host. It also demonstrates the high degree of zoning of augite. Using Lindsley's pyroxene thermometer [13], the compositions of pyroxenes point to igneous closure temperatures of ∼850°C for augite rims and ∼950°C for cores.

We observe two basic modes of deformation in pyroxenes: intensive glide and mechanical twinning both on (100) planes (Fig. 5A,B). The specific mechanism being activated may depend on the orientation of pyroxene with respect to the shock direction. The predominant deformation feature in augites adjacent to the thin (1 μm) vein are numerous glide bands parallel (100). Since augite and pigeonite can both glide on (100)[001] and (100)[010] slip systems, the glide bands cross the epitactically exsolved pigeonite lamellae, shearing and offsetting them (Figs. 3 and 5A). This results in a zigzag pattern of the pigeonite lamellae. Very thin amorphous veins occur occasionally along slip planes and at pigeonite–augite interfaces (Fig. 5A). At the contact to the veins, pigeonite lamellae are completely amorphous while augite is still crystalline, suggesting a lower melting temperature of pigeonite. The augite is, however, not completely crystalline; it is transected by many thin (<20 nm) amorphous veins parallel to the (100) glide plane.
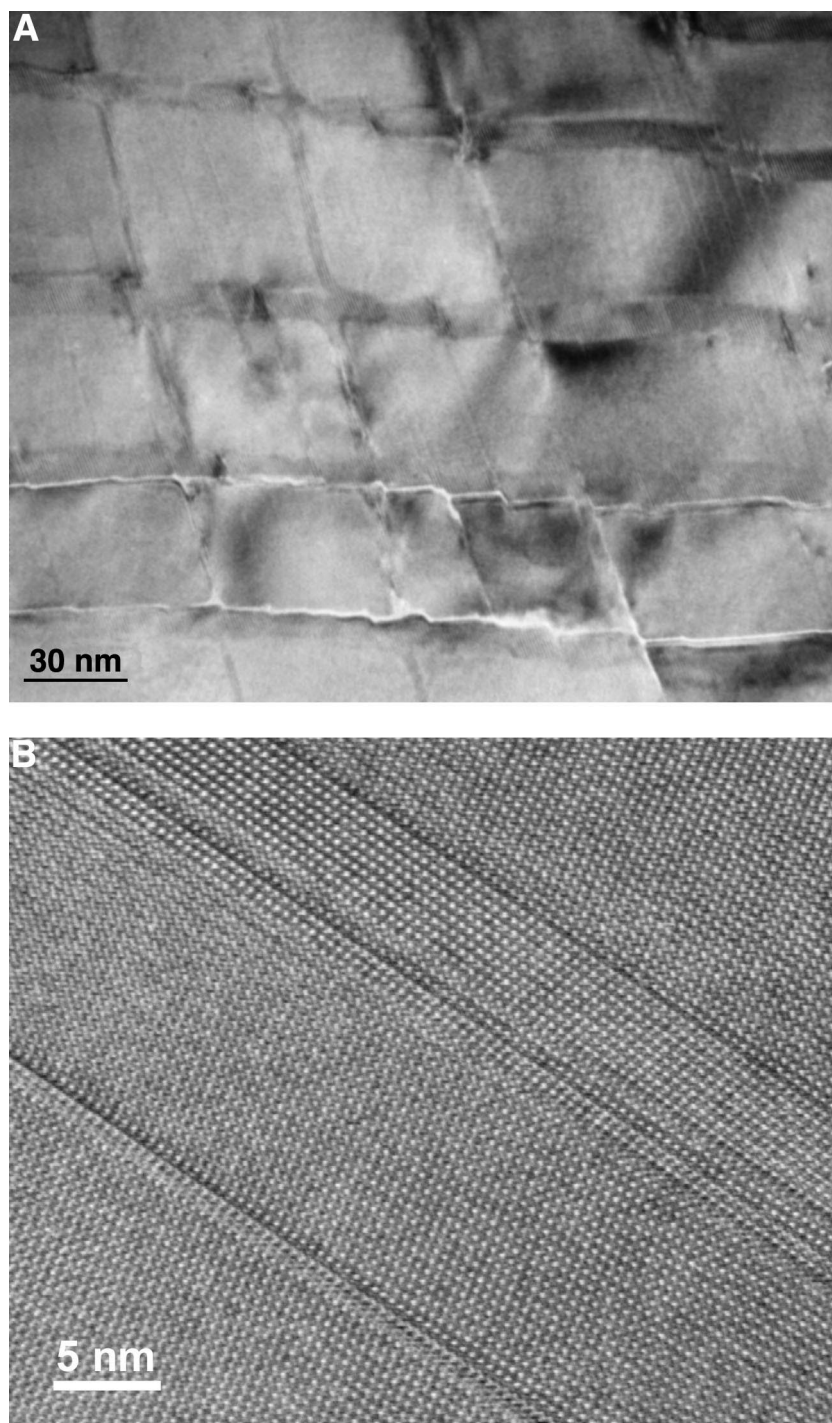
Fig. 5. (A) HRTEM image of augite with pigeonite exsolution lamellae. The zigzag pattern of pigeonite–augite interfaces results from the activation of glide bands parallel to (100). Note the thin films of amorphous material along the glide bands and at interfaces. (B) HRTEM image of an augite crystal, containing numerous mechanical twins parallel to (100). The [011] zone axis of augite is parallel to the beam.
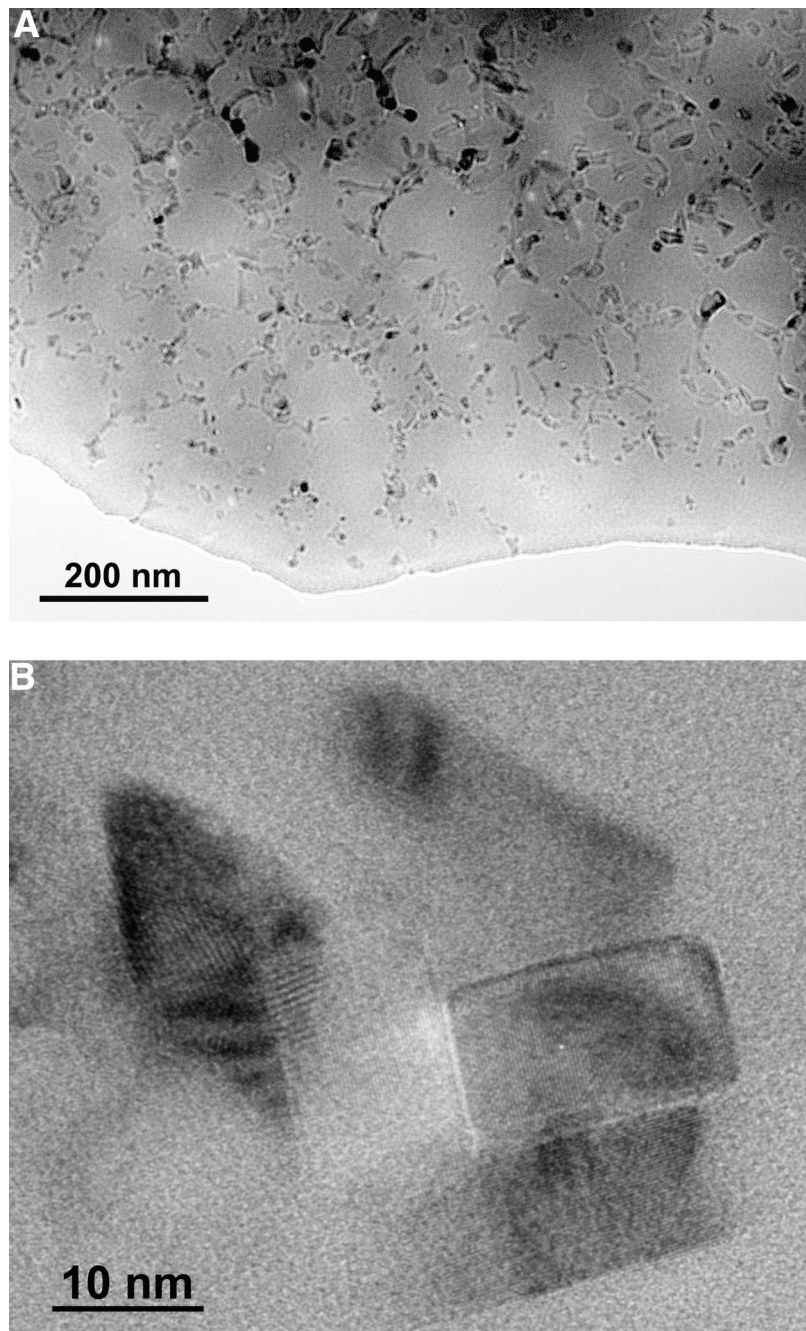
Fig. 6. (A) Highly defocused bright field TEM image of the typical microtexture within the thin (1 μm) melt vein. Amorphous, equant-shaped areas probably represent perovskite, which amorphized during decompression. These perovskite grains are surrounded by tiny wüstite and stishovite precipitates. (B) HRTEM image of stishovite (rectangular shape) and wüstite grains.

The microtexture of the 1 μm wide vein adjacent to augite is distinctly different from that of the 100 μm wide vein described above and in [5]. It typically consists of a loose network of small (< 10 nm) crystals of wüstite and stishovite (Fig. 6), the latter easily recognizable by their characteristic needle shape as well as their electron diffraction patterns and microanalyses (Fig. 4b). The network encloses amorphous domains, of size typically ranging from 50 to 200 nm. The general appearance is suggestive of that of a polycrystal, with grain boundaries meeting at angles close to 120°, in textural equilibrium, decorated with intergranular stishovite and wüstite precipitates (Fig. 6A,B). Here, however, the 'grains' are amorphous.

EDX microanalyses of these amorphous 'grains' show variable Mg, Fe, and Ca contents but all analyses fit compositionally to an ABO_3 formula typical of pyroxene or silicate perovskite with A = Mg, Fe, and Ca and B = Si (Table 1, Fig. 4). Their $(Mg_{0.25-0.3}Fe_{0.3-0.4}Ca_{0.3-0.35})SiO_3$ compositions are scattered between those of adjacent augite $(Mg_{0.3}Fe_{0.3}Ca_{0.4})SiO_3$ and pigeonite lamellae $(Mg_{0.25}Fe_{0.55}Ca_{0.1})SiO_3$ (Fig. 4). The Mg/Fe ratio of the amorphous 'grains' is similar to that in adjacent pyroxene, suggesting that the melt reflects the local composition of adjacent pyroxene. In some analyses Si and Ti add up to ~ 1, suggesting a replacement of Si by Ti in the $(Mg,Fe,Ca)(Si,Ti)O_3$ formula (Table 1). The vein region richer in Ti also contains more Fe, which may indicate that a small ilmenite inclusion in pyroxene was locally incorporated and mixed into the melt.

X-ray elemental mapping has been used to spatially image the compositional heterogeneity of major elements within the vein and of the amorphous 'grains'. Heterogeneity is observed in Ca and Fe maps, revealing a correlation between
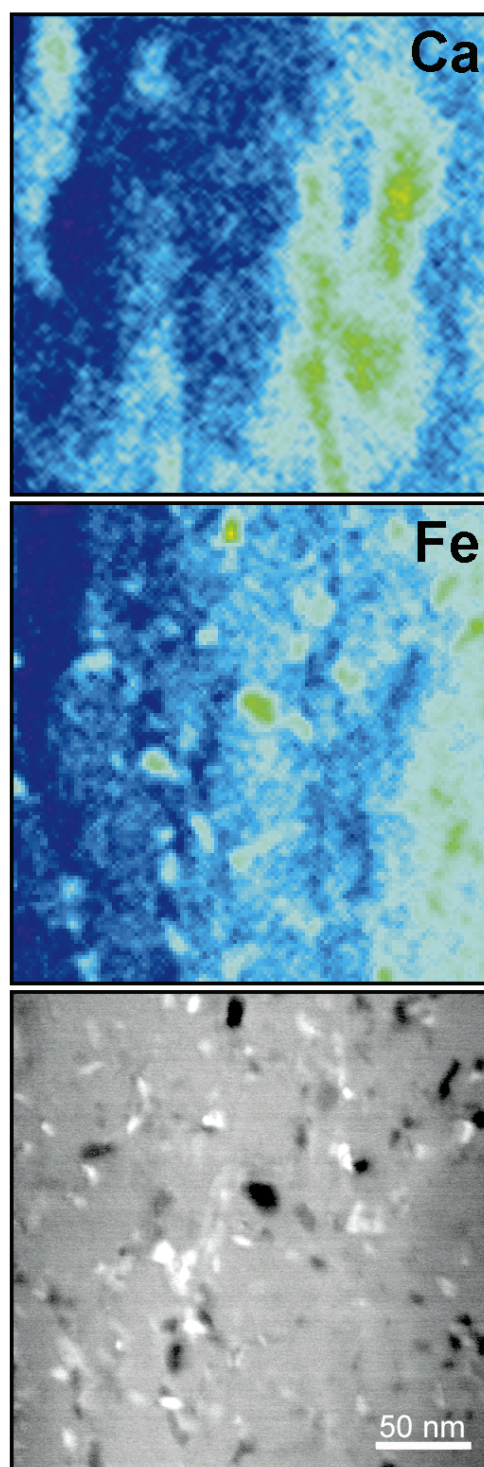
$\rightarrow$

Fig. 7. X-ray Ca and Fe distribution maps and corresponding dark field STEM image of a heterogeneous region within the vein. Fe-rich areas correspond to the tiny wüstite precipitates; the schlieren texture in the Ca map reflects an inherited feature of the melted augite with pigeonite exsolutions. Green corresponds to the highest concentration, blue to the lowest.
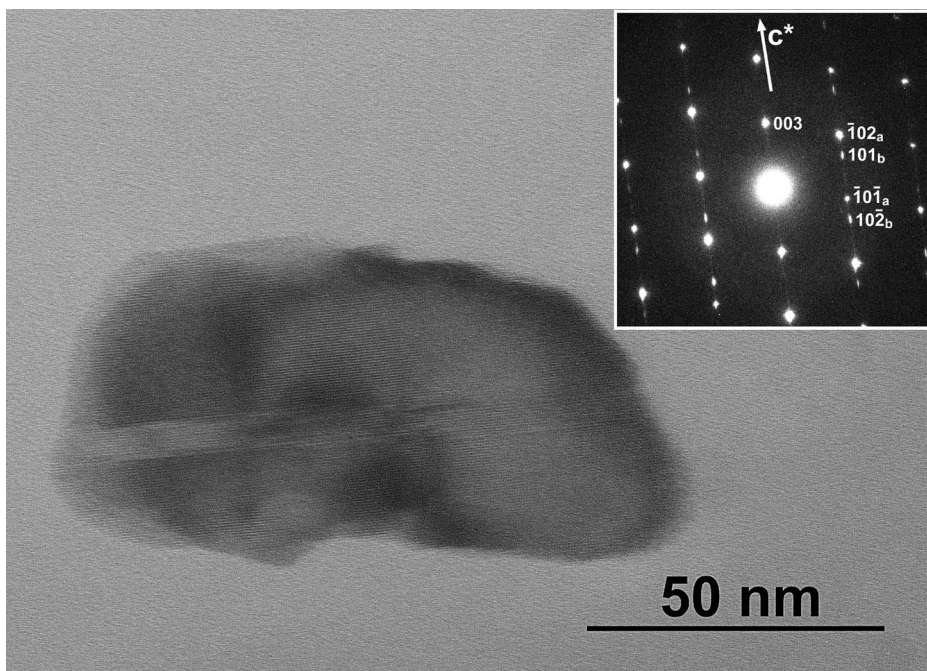
Fig. 8. HRTEM image of a tiny akimotoite grain embedded in glassy silicate material. A 10 nm wide twin lamellae parallel to (0001) is transecting the ilmenite-structured grain. The inset shows the corresponding electron diffraction pattern displaying the different orientations of twin *b* and host *a*.

the two elements, i.e. the vein is locally richer in Fe and poorer in Ca, or vice versa (Fig. 7). The presence of wüstite is easily recognized in such elemental maps due to its high Fe content. Within the detection limits, we could not observe a compositional variation in the amorphous grains, but at a larger scale of a few 100 nm, a schlieren texture is commonly observed, with streaks relatively rich in Ca and poor in Fe and vice versa (Fig. 7). This heterogeneous distribution of Ca and Fe is obviously an inherited feature of the precursor augite and its pigeonite exsolution lamellae. Due to the short time scale of the shock event, the frictional melt was apparently only incompletely mixed, preserving the compositional heterogeneity of the precursor pyroxene.

Besides the amorphous 'grains', two additional crystalline phases of similar size (~ 100 nm) occur subordinately in the vein. One phase was found to be Ca-poor, with a composition close to that of enstatite $(Mg_{0.64}Fe_{0.31}Ca_{0.01})SiO_3$ (Table 1, Fig. 4a,b). As shown in Fig. 8, this phase, about

100×50 nm in size, contains sometimes thin twin lamellae and is embedded in the amorphous material. The electron diffraction pattern is compatible with the ilmenite structure (inset in Fig. 8) and indicates that the twin plane is (0001), a typical twin orientation for this structure. The *d*-spacings determined from the inset in Fig. 8 are 4.54 Å (003) and 3.95 Å (101). Using these values we obtain the following lattice constants: $a = 4.76$ Å, $c = 13.62$ Å. The absolute *a* and *c* values, the *c/a* ratio, and the compositional data altogether support the identification of the Ca-poor crystals as akimotoite, the high-pressure phase of enstatite, recently discovered in *L5-6* chondrites [14–16].

The other crystalline phase, found in the same region of the vein, is richer in Si than pyroxenes, with a composition close to $(Mg_{0.4}Fe_{0.4}Ca_{0.2})Si_2O_5$ (Figs. 4b and 9, and Table 1). Finger and Hazen [17] predicted that Si may replace Ti at high pressure in phases with pseudo-brookite $(FeTi_2O_5)$ or titanite (sphene) $(CaTiSiO_5)$ structure. A natural
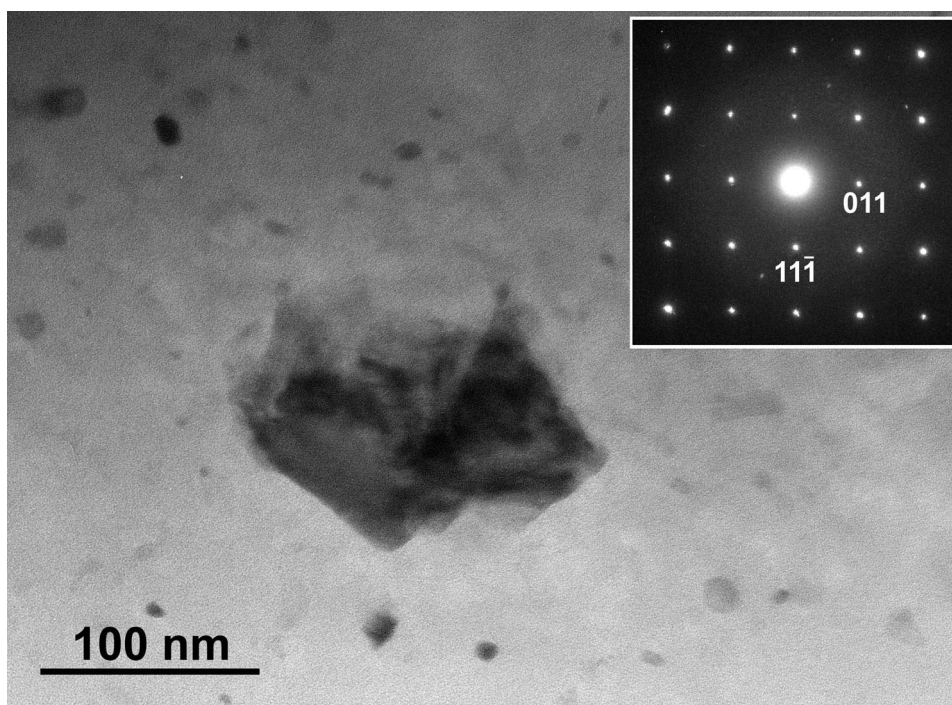
Fig. 9. Bright-field TEM image of a silicate titanite grain and corresponding electron diffraction pattern taken along the [2$\bar{1}$1] zone axis (inset). The amorphous matrix contains numerous wüstite and stishovite grains.

$(Mg_{0.5}Fe_{0.5})Ti_2O_5$ pseudobrookite is known as the orthorhombic mineral armalcolite and was first identified in lunar basalt samples [18,19] and later found in terrestrial lamproites [20]. Ferro-magnesian silicate armalcolite is, so far, unknown but could be a stable high-pressure phase. On the other hand, it has been experimentally shown that Si can entirely replace Ti at high pressures in the monoclinic titanite structure, and $CaSi_2O_5$ and $MnSi_2O_5$ have been synthesized at pressures of about 10 GPa [21–23]. Natural calcic silicate titanite has also been found as inclusion in kimberlite diamonds [24]. By tilting the sample under the electron beam, we obtained five different diffraction patterns on a single crystal. They could not be indexed in the orthorhombic system, and were only compatible with a monoclinic lattice, ruling out an identification of the phase as armalcolite. Zone axis directions and reciprocal vectors observed within the zone axis patterns are plotted in a stereogram (Fig. 10), showing the angular relationship between all observed directions in re-

ciprocal space. Both angles in reciprocal space and d-spacings are fully compatible with the titanite structure (Table 2). Systematic absence of reflections with $k+l=2n+1$ additionally show that the space group is $A/2a$, i.e. the high-pressure space group of calcic silicate titanite [21,22]. The refinement yields the following lattice constants: $a = 6.53$ Å, $b = 8.20$ Å, $c = 6.45$ Å, $\beta = 115.5°$ (Table 2). These constants are close to those found for $MnSi_2O_5$, for which $\beta = 114.5°$ [23]. To our knowledge, it is the first time that a ferro-magnesian silicate with titanite structure has been reported.

4. Cooling and freezing of the molten veins

Any attempt to interpret the observations must involve assumptions on the time required to solidify the veins during the high-pressure phase of the shock. Several arguments support the suggestion that the veins solidified by crystallization from the

liquidus, rather than by quenching through the glass transition temperature. The presence of numerous idiomorphic crystals in the veins points to crystallization from the melt, whereas later devitrification of a glass would have produced a spherulitic, dendritic, or microcrystalline fibrous texture [25]. Indeed, heterogeneous nucleation probably occurred very fast near the edge of the veins and crystallization, once started, entirely precluded supercooling of the liquid to form a glass. Also, the microtexture of the amorphous 'grains' suggests that they initially were crystalline (Fig. 6A).

However, it is not immediately obvious whether all crystals, especially the tiny precipitate-like wüstite and stishovite crystals, were formed by crystallization from the melt or whether some subsequent solid-state precipitation occurred. The time for diffusion of ions over distances of

Table 2
d-spacings and lattice parameters of ferro-magnesian silicate titanite (Table 1)

h	k	l	d_{obs} (Å)	d_{calc} (Å)
0	1	1	4.74	4.75
1	1	−1	4.55	4.56
1	2	0	3.37	3.36
1	0	−2	3.22	3.22
0	0	2	2.94	2.91
1	2	−2	2.53	2.53
1	3	−1	2.46	2.45
1	3	1	2.15	2.14
1	4	0	1.92	1.94
0	1	3	1.91	1.89
1	4	−2	1.72	1.73
1	3	−3	1.70	1.68
2	3	−3	1.67	1.66
2	4	−2	1.65	1.64
1	4	2	1.50	1.52
2	2	−4	1.48	1.50
2	5	−1	1.47	1.46

a (Å) 6.53(9)
b (Å) 8.20(7)
c (Å) 6.45(4)
β (°) 115.5(8)
V (Å^3) 311.6(9.8)

The *d*-spacings have been determined on a single crystal using five selected area electron diffraction patterns (see Figs. 9 and 10). Errors in lattice parameters *a*, *b*, *c*, *V*, and *β* are 1σ.
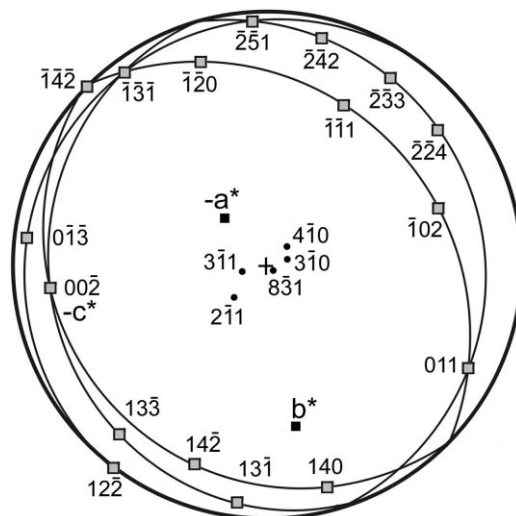

Fig. 10. Stereoplot showing the orientation of reciprocal vectors within the electron diffraction patterns (open squares) that were recorded along five zone axes (filled circles) of silicate titanite. As a reference, the orientation of the *a**, *b**, and *c** axes is given, which were not accessible due to the limited tilt angles (±25°). The angular relationship between reciprocal vectors is fully compatible with the titanite structure.

the order of the typical crystal sizes (5–200 nm) must therefore be compared to the time for cooling and crystallization of the vein (see Section 5).

An estimate of the temperature evolution in the vein and the adjacent matrix during crystallization, as well as the time required for complete solidification can be obtained by viewing the vein as a thin slab of width 2*w*, bound by two semi-infinite half-spaces. Initially, the material in the vein is liquid, at its melting point T_m or higher, and the wall rock, on either side is solid, at temperature T_0. The liquid cools, crystallizes and releases the latent heat of melting. The solidification front moves into the vein, and the thickness of the solidified layer (counted from the wall) is obtained by postulating that the latent heat released at the advancing front is conducted away toward the wall and into the colder matrix. This is the so-called Stefan problem (see e.g., [26], pp. 172–174). The vein becomes entirely solid when the fronts from each side of the vein meet in the middle. The time for complete solidification t_s is
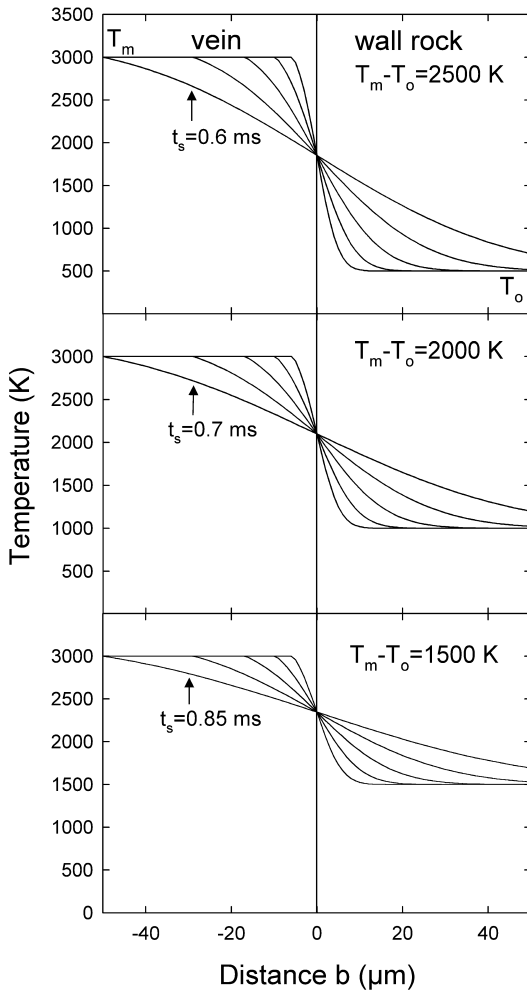
Fig. 11. Evolution of temperature as a function of the distance from the contact between the wall rock and the 100 μm wide melt vein (b = at contact). Three diagrams are shown for initial temperature differences $T_m - T_0$ of 2500, 2000, and 1500 K. The temperature profiles within each diagram are calculated for times $t = t_s/3^x$ with x = 0, 1, 2, 3, and 4. The initial temperature in the melt T_m was set to the constant value of 3000 K; T_0 was assumed to be 500, 1000, and 1500 K.

found by solving the Stefan problem; it is given by:

$$ t_s = \frac{w^2}{4\kappa\lambda^2} $$

where w is the half-width of the slab, κ is the thermal diffusivity of the solidified vein and the

surrounding rock, and λ is a dimensionless coefficient, given by:

$$ \lambda = \frac{\delta}{2\sqrt{\kappa t}} $$

where δ is the thickness of the solidified layer, on either side of the vein, at time t. The value of λ is obtained, from the boundary condition at the moving front, by solving the transcendental equation:

$$ \frac{L\sqrt{\pi}}{C_p(T_m - T_0)} = \frac{e^{-\lambda^2}}{\lambda(1 + \text{erf}\,\lambda)} $$

where L is the latent heat of solidification, C_p is the specific heat at constant pressure, and erf is the error function. The temperature at the walls T_w of the vein stays constant during solidification and its value is:

$$ T_w = T_0 + \frac{T_m - T_0}{1 + \text{erf}\,\lambda} $$

If we take typical values: L = 320 kJ/kg, C_p = 1.2 kJ/kg K, $\kappa = 10^{-6}$ m²/s, and $T_m - T_0 = $ 2500 K, we find λ = 1.02. It follows that for veins 1, 10, 100 μm wide, the time to complete solidification t_s is about 60 ns, 6 μs, and 0.6 ms, respectively (Figs. 11 and 12). This time estimate is not very sensitive to $T_m - T_0$, if it is sufficiently large (> 500 K). For example, the solidification time for $T_m - T_0$ = 2500 K differs from the time for $T_m - T_0$ = 1500 K by a factor 0.7 only for all vein thicknesses (Fig. 11). The thickness of the vein exerts, however, an important control on the solidification time t_s (Fig. 12): for $T_m - T_0$ = 2000 K, for example, we obtain solidification times t_s of 70 ns, 7 μs, 0.7 ms, and 70 ms for veins 1 μm, 10 μm, 100 μm, and 1 mm wide, respectively (Fig. 12); cooling and solidifying a 1 mm wide vein would thus require a time eight orders of magnitude longer than for a 1 μm wide vein. While thin veins are typical of Zagami, shocked ordinary chondrites (e.g. *L6* chondrites) commonly contain millimeter thick veins with abundant high-pressure phases. A simple explanation for this difference could be that, compared to Mars, the parent body of ordinary chondrites collided with a dis-

tinctly larger projectile resulting in a longer shock duration.

We have assumed that crystallization proceeds without hindrance, as soon as the temperature becomes equal to the melting point, due to the ease of nucleation. At the end of solidification, the temperature at the walls is very close to T_0 $(T_m - T_0)/2$ (Fig. 11). Assuming that at the moment of the shock, the temperature of the rock was $T_0 \sim 500$ K, the temperature at the walls at the end of solidification of the vein, was about 1850 K, decreasing away from the vein inside the rock. It is not possible to know the cooling history of the meteorite beyond the time of complete solidification of the veins, since the boundary conditions of the problem are unknown. We can only surmise that, since heat must be evacuated through the bulk of the rock, the veins and the regions close to them will cool down at a rate slow enough to allow diffusion to take place locally.

To judge whether adiabatic cooling during decompression could significantly influence the cooling history of veins, we can estimate its effect from:

$$\left(\frac{d\ln T}{d\ln \rho}\right)_s = \gamma$$

where T is the temperature, ρ the density and γ the Grüneisen parameter [27]. Using the approximation:

$$\Delta T = \Delta \rho \frac{T}{\rho} \gamma$$

and taking estimated values of the Grüneisen parameter $\gamma = 1.2$, of the post-shock bulk temperature $T \sim 500$ K, and of the density of pyroxenes at the shock pressure of 30 GPa, $\rho + \Delta\rho = 3930$ kg/m³, and at ambient pressure, $\rho = 3330$ kg/m³ [28] we find that the adiabatic drop in bulk temperature during the total time of decompression is $\Delta T \sim 110$ K. A higher post-shock temperature would not significantly enhance the amount of adiabatic cooling. For example, assuming a post-shock temperature of 1000 K, the temperature decrease due to adiabatic cooling would be
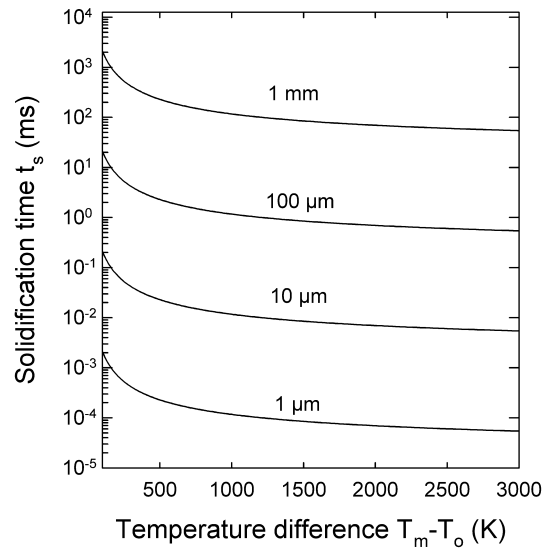

Fig. 12. Solidification time t_s as a function of the initial temperature difference $T_m - T_0$ at the contact between the wall rock and the vein. Calculations are shown for four different vein thicknesses of 1, 10, 100 μm, and 1 mm.

$\Delta T \sim 220$ K. If quenching of the veins occurs during decompression, the adiabatic contribution to the cooling of the veins is almost negligible. Adiabatic cooling is also not likely to affect very much the time during which the solidified veins stay at temperatures high enough for solid-state diffusion to be effective (see Section 5).

5. Diffusion and solid-state precipitation in the vein

To precipitate tiny minerals such as wüstite or stishovite from a parent high-pressure phase, diffusion of ions must be possible over distances comparable to the size of crystals (10–100 nm), during the time that the vein is still at high temperature. The diffusion coefficients in the relevant high-pressure minerals are unknown, but we can make educated guesses, using known values of diffusion coefficients in some minerals.

The characteristic time τ for diffusion of a species over the distance d is:

$$\tau = \frac{d^2}{D} = \frac{d^2}{D_0 \exp\left(-\frac{\Delta H}{RT}\right)}$$

where D is the diffusion coefficient, D_0 is a pre-exponential coefficient, ΔH is the activation enthalpy and R is the gas constant. The diffusion coefficient of oxygen in forsterite at ambient pressure [29] can be taken as a upper bound, with $D_0 = 6.7 \times 10^{-6}$ m²/s and $\Delta H = 318$ kJ/mol. For a lower bound, we can take the diffusion coefficient of silicon in silicate perovskite at 25 GPa [30], with $D_0 = 2.7 \times 10^{-10}$ m²/s and $\Delta H = 336$ kJ/mol. Characteristic times for diffusion can then be estimated. Over a distance of 5 nm (typical of most wüstite and stishovite crystals in the 1 μm wide vein) and at $T = 3000$ K, the upper bound is about 60 ms, while the lower bound is of the order of 1 μs. At $T = 1850$ K, the bounds on characteristic times are 4 min and 3 ms. It is, therefore, not unreasonable to assume that a vein, once rapidly solidified, may cool down from the melting temperature to the temperature that the wall had during solidification, in times of the order of seconds, during the decompression phase. It should then be possible for minerals crystallized at high pressure to decompose to tiny (~ 5 nm) phases more stable at lower (but still high) pressure, by diffusion in the solid-state.

Over distances of 100 nm (typical size of the akimotoite and titanite grains), the characteristic diffusion time may take values between 0.4 ms and 24 s at 3000 K and 1 s and 28 h at 1850 K. Solid-state diffusion probably cannot occur on this length scale within the short time span of the shock event, which supports the contention that the high-pressure phases akimotoite and titanite have formed during primary crystallization.

6. Discussion

Based on the observations and calculations, we may now suggest a scenario for the formation and evolution of the veins and the high-pressure crystals therein.

As the shock pressure rises steeply, deviatoric stresses cause plastic deformation and cracking in minerals and at grain boundaries. Local shear heating due to friction along cracks or concentration of shear in glide bands may result in melting. This may also happen during the decompression stage, if the deviatoric component of the stress tensor decreases less rapidly than the hydrostatic pressure. The formation of the melt veins is thus simply a consequence of the deviatoric component rather than the result of pressure heterogeneities. The observation of 10 nm wide amorphous films in (100) glide bands crossing augite adjacent to the main black vein is compatible with the idea that the increase in temperature caused by localized plastic deformation at very high strain rates is sufficient to bring about melting. It is also possible that dislocations may act as preferential sites for melting, as suggested by the observation of very thin amorphous films along slip planes in pigeonite lamellae (Fig. 5A). At the rim of veins, preferential melting of pigeonite is observed, suggesting a melting temperature lower than that of augite.

Shear melting, as in pseudotachylites [31], must take place at an extremely fast rate, and complete crystallization of very thin layers of melt must occur almost immediately in times probably < 1 ms. This is a conservative time estimate, taking into account the uncertainties in temperatures entering the modeling of the cooling and solidification process. As in pseudotachylites, there is no time for mechanical mixing [31] and this accounts for the existence of considerable compositional heterogeneity in the 1 μm wide vein, with schlieren features and regions richer or poorer in Ca and Fe, inherited from neighboring grains of augite or pigeonite. An additional reason for the preservation of chemical heterogeneity is that diffusion can only take place over short distances (< 100 nm), insufficient to equilibrate the composition of the entire vein. The fact that the veins are almost completely crystalline may be accounted for by very rapid nucleation, leading to fast crystallization controlled only by the evacuation of heat. The almost instantaneous crystallization of the melt formed by shear prevents the shear stress from relaxing and additional melting may therefore occur. If the kinetics of crystallization are more rapid than that of shear heating, shearing continues and could cause repetitive melting and crystallization, leading to a thickening of the vein. If crystallization occurs during the decompression, one would also expect the veins to

be somehow 'zoned', with the edges reflecting different pressures and temperatures than the center of the vein. Indeed, in the central part of the 100 μm wide veins, we find mineral assemblages that are indicative of higher pressure than those at the margins. The polycrystalline hollandite aggregates in the center of the vein record pressures < 23 GPa [5,9], whereas pyroxenes observed in the margins may have formed at pressures < 10 GPa [5].

Consistent with the calculations, the mineralogical and microtextural observations in the 1 μm thin vein point to a high cooling rate and indicate rapid crystallization of the vein in a single event at high pressure. Using shock barometers [32], the peak shock pressure in Zagami was estimated to be of the order of 30 GPa [4,5]. The stable phase that could crystallize at pressures > 24 GPa [33] from the incompletely mixed melt is perovskite. Due to the high crystallization temperatures the perovskite could assimilate large amounts of Ca and show compositions between that of adjacent augite and pigeonite. Several lines of arguments support the hypothesis that the amorphous 'grains', the predominant phase in the vein, have indeed been perovskites at high pressure and amorphized upon decompression:

1. The microtexture, with numerous precipitates decorating the 'grain' boundaries that meet at 120° angles, resembles that of an annealed polycrystal.
2. Amorphization is a known decompression effect of perovskite, especially if Ca is a constituent. Amorphous 'perovskites' have previously been observed in a shocked L chondrite [16].
3. Coexisting phases of similar size such as akimotoite record high pressures.
4. The isovalent replacement of octahedrally coordinated Si by Ti is known to occur in the perovskite structure (see analysis (5) in Table 1). However, in the isochemical pyroxene structure with tetrahedrally coordinated Si, the Ti replaces only cations on M sites.

As pressure dropped after a time that depends on the unknown size of the impactor, but which could be of the order of a few seconds, temperature, although decreasing, remained high enough in the veins for solid-state diffusion to take place. Perovskite crystals could have then tended toward the equilibrium mineral assemblage at lower pressure and temperature [33], by exsolving wüstite FeO and SiO_2, in its high-pressure form, stishovite. The precipitation of these crystals would occur at grain boundaries, forming the loose network observed. The diffusion calculations fully support this model and indicate that solid-state diffusion can occur within seconds over distances similar to the size of wüstite and stishovite crystallites. The residual perovskite grains would have then become Mg-richer and thus more stable at that pressure. However, as temperature continued to decrease, exsolution stopped, and as pressure decreased as well, the Ca-bearing perovskite, not metastable at atmospheric pressures, could have amorphized. Idiomorphic crystals of akimotoite and silicate titanite occur subordinately in the thin vein, as well, and have grain sizes (~ 100 nm) similar to those of 'perovskite', which suggests that both akimotoite and silicate titanite have crystallized from a high-pressure melt, as well. This is supported by the diffusion calculations, which basically rule out that both phases could be the products of solid-state diffusion. By the time crystals could grow to a size of 100 nm by solid-state diffusion, the pressure would presumably have decreased considerably or the transient shock event could have been over.

It is also unlikely that the $(Mg_{0.6}Fe_{0.3})SiO_3$ akimotoite is a product of solid-state inversion from perovskite. Diamond anvil cell experiments have shown that perovskite transforms back to a $LiNbO_3$-structured phase (space group R3c) and not to akimotoite (ilmenite structure; $R\bar{3}$) [34]. The inversion to the $LiNbO_3$ structure causes polysynthetic twinning parallel to $(10\bar{1}2)$. We observe occasionally twins but parallel to (0001), which is a common orientation of growth twins in ilmenite. Additionally, diffraction patterns neither show systematic absence due to c-glide planes nor does the c/a ratio of 2.86 fit to the $LiNbO_3$ structure [34], i.e., the space group and lattice dimensions are fully compatible with the ilmenite structure ($R\bar{3}$, Fig. 8).

The ferro-magnesian silicate titanite of approx-

imate composition $(Mg_{0.4}Fe_{0.4}Ca_{0.2})Si_2O_5$ has never been observed before in any rock. Recently, a natural Ca analogue, $CaSi_2O_5$ titanite, has been discovered as inclusion in a kimberlite diamond [24]. The ferro-magnesian silicate titanite possesses the high-pressure $A2/a$ symmetry. The structure of $A2/a$ titanite consists of parallel chains of edge-sharing SiO_6 octahedra (TiO_6 in $CaTiSiO_5$ titanite) bridged by edge-sharing SiO_4 tetrahedra [22,23]. The metallic cations are located in distorted MO_7 polyhedra. The fact that silicon is not entirely octahedrally coordinated accounts for the lack of stability of silicate titanite at very high pressures. Indeed, $CaSi_2O_5$ silicate titanite has been found to be stable between approximately 8 and 15 GPa at 1350°C and to decompose into Ca perovskite and stishovite at higher pressures [22]. $MnSi_2O_5$ silicate titanite was synthesized at 11 GPa, but its stability at higher pressures is not known [23]. Pressures and temperatures of syntheses are similar to those expected in Earth's transition zone, where ferro-magnesian titanite could be an important constituent.

The unit cell volume at ambient pressure of ferro-magnesian silicate titanite $(Mg_{0.4}Fe_{0.4}Ca_{0.2})$-$Si_2O_5$ is slightly smaller than that of $CaSi_2O_5$ (311.6 Å^3 versus 320.1 Å^3 [21]). As the molar weights of both phases are almost identical ($M = 176$–177 g/mol), it follows that ferro-magnesian silicate titanite ($\rho = 3.78$ g/cm^3) is about 3% denser at atmospheric pressure than calcic silicate titanite ($\rho = 3.66$ g/cm^3). This suggests that it is stable at pressures as high or even higher than those of $CaSi_2O_5$.

A ferro-magnesian 'high-silica phase' was reported in recovered samples of olivine, laser-heated in a diamond anvil cell at a nominal pressure of 50 GPa, and examined by TEM [35]. The phase was observed in the center of the laser-heated stripes, where temperature was highest, possibly close to 2500 K. The authors suggested that the phase might form by the breakdown of silicate perovskite at high temperature. In our case, however, the diffusion calculations and the microstructural similarities to akimotoite and 'perovskite' basically rule out the possibility that the ferro-magnesian titanite could result from a breakdown at high temperature of ferro-magnesian silicate perovskite into titanite and magnesio-wüstite, as suggested in [35]. It is more likely that they were formed during primary crystallization from the melt in high-temperature and silica-rich regions of the veins. Experimental investigations are needed to establish the stability domain in temperature and pressure of the ferro-magnesian silicate titanite.

7. Conclusions

The investigation of the microstructure of black veins in the Zagami meteorite, using analytical electron microscopy, has revealed the existence of several high-pressure minerals: stishovite, K- and Na,Ca-rich hollandites, akimotoite, and ferro-magnesian silicate titanite, as well as amorphous 'perovskite'.

The veins are thought to form by melting due to shear heating; their heterogeneous composition reflects the diversity of the local minerals they cut, leading to the formation of different high-pressure minerals. Estimates of crystallization times for veins of various thicknesses, and of solid-state diffusion times characteristic for relevant elements, are compatible with the conclusion that the high-pressure minerals observed in the vein crystallized in extremely short times, much shorter than the duration of the shock. Due to the very high temperatures, perovskite could subsequently evolve, by solid-state diffusion, toward its lower pressure assemblage wüstite+stishovite.

Beyond the PTt path in the impact event, our investigation may also provide important clues to the mineralogy of planetary interiors. The coexistence of ferro-magnesian silicate titanite with akimotoite and 'perovskite' suggests a formation at similar high pressures and very high temperatures close to the liquidus. The crystal structure of titanite with mixed coordination of Si is intermediate between upper and lower mantle structures with purely tetrahedral or octahedral coordination of Si. The structure is also known to be a carrier of radioactive elements. Thus, silicate titanite could be an important constituent in Earth's transition zone, containing

a large portion of the radioactive inventory at this depth.

Acknowledgements

References

[1] H.Y. McSween Jr., What we have learned about Mars from SNC meteorites, Meteoritics 29 (1994) 757–779.

[2] K. Marti, J.S. Kim, A.N. Thakur, T.J. McCoy, K. Keil, Signatures of the Martian atmosphere in glass of the Zagami meteorite, Science 267 (1995) 1981–1984.

[3] T.J. McCoy, G.J. Taylor, K. Keil, Zagami: Product of two-stage magmatic history, Geochim. Cosmochim. Acta 56 (1992) 3571–3582.

[4] F. Langenhorst, D. Stöffler, D. Klein, Shock metamorphism of the Zagami achondrite, Lunar Planet. Sci. XXII (1991) 779–780.

[5] F. Langenhorst, J.P. Poirier, 'Eclogitic' minerals in a shocked basaltic meteorite, Earth Planet. Sci. Lett. 176 (2000) 259–265.

[6] E. van Cappellen, J.C. Doukhan, Quantitative X-ray microanalysis of ionic compounds, Ultramicroscopy 53 (1994) 343–349.

[7] E. van Cappellen, The parameterless correction method in X-ray microanalysis, Microsc. Microanal. Microstruct. 1 (1990) 1–22.

[8] F. Langenhorst, P. Joreau, J.C. Doukhan, Thermal and shock metamorphism of the Tenham chondrite: A TEM examination, Geochim. Cosmochim. Acta 59 (1995) 1835–1845.

[9] A. Yagi, T. Suzuki, M. Akaogi, High pressure transitions in the system $KAlSi_3O_8$–$NaAlSi_3O_8$, Phys. Chem. Miner. 21 (1994) 12–17.

[10] P. Gillet, M. Chen, L. Dubrovinsky, A. ElGoresy, Natural $NaAlSi_3O_8$-hollandite in the shocked Sixiangkou meteorite, Science 287 (2000) 1633–1636.

[11] W.F. Müller, Thermal and deformation history of the Shergotty meteorite deduced from clinopyroxene microstructure, Geochim. Cosmochim. Acta 57 (1993) 4311–4322.

[12] S. Weinbruch, W.F. Müller, Constraints on the cooling rates of chondrules from the microstructure of clinopyroxene and plagioclase, Geochim. Cosmochim. Acta 59 (1995) 3221–3230.

[13] D.H. Lindsley, Pyroxene thermometry, Am. Mineral. 68 (1983) 447–493.

[14] N. Tomioka, K. Fujino, Natural $(Mg,Fe)SiO_3$ ilmenite and perovskite in the Tenham meteorite, Science 277 (1997) 1084–1086.

[15] N. Tomioka, K. Fujino, Akimotoite, $(Mg, Fe)SiO_3$ a new silicate mineral of the ilmenite group in the Tenham meteorite, Am. Mineral. 84 (1999) 267–271.

[16] T.G. Sharp, C. Lingemann, C. Dupas, D. Stöffler, Natural occurrence of $MgSiO_3$-ilmenite and evidence for $MgSiO_3$-perovskite in a shocked L chondrite, Science 277 (1997) 352–355.

[17] L.W. Finger, R.M. Hazen, Crystal chemistry of six-coordinated silicon: a key to understanding the Earth's deep interior, Acta Cryst. B47 (1991) 561–580.

[18] A.T. Anderson, T.E. Bunch, E.N. Cameron, S.E. Haggerty, F.R. Boyd, L.W. Finger, O.B. James, K. Keil, M. Prinz, P. Ramdohr, A. El Goresy, Armalcolite: A new mineral from the Apollo 11 samples, Proc. Apollo 11 Lunar Sci. Conf. 1 (1970) 55–63.

[19] J.R. Smyth, The crystal chemistry of armalcolites from Apollo 17, Earth Planet. Sci. Lett. 24 (1974) 262–270.

[20] D. Velde, Armalcolite–Ti–Phlogopite–Diopside–Analcite-Bearing Lamproites from Smoky Butte, Garfield County, Montana, Am. Mineral. 60 (1975) 566–573.

[21] R.J. Angel, N.L. Ross, F. Seifert, T.F. Fliervoet, Structural characterization of a pentacoordinate silicon in a calcium silicate, Nature 384 (1996) 441–444.

[22] R. Knoche, R.J. Angel, F. Seifert, T.F. Fliervoet, Complete substitution of Si for Ti in Titanite $Ca(Ti_{1-x}Si_x)^{VI}Si^{IV}O_5$, Am. Mineral. 83 (1998) 1168–1175.

[23] T. Arlt, T. Armbruster, P. Ulmer, T. Peters, $MnSiO_2O_5$ with titanite structure: A new high pressure phase in the MnO–SiO_2 binary, Am. Mineral. 83 (1998) 657–660.

[24] W. Joswig, T. Stachel, J.W. Harris, W.H. Baur, G.P. Brey, New Ca-silicate inclusions in diamonds-tracers from the lower mantle, Earth Planet. Sci. Lett. 173 (1999) 1–6.

[25] A. Spry, Metamorphic textures, Pergamon, 1969, 350 pp.

[26] D.L. Turcotte, G. Schubert, Geodynamics, J. Wiley and Sons, 1982, 450 pp.

[27] J.P. Poirier, Introduction to the Physics of the Earth's Interior, 2nd. edn., Cambridge University Press, Cambridge, 2000, 312 pp.

[28] S.P. Marsh, LASL Shock Hugoniot data, University of California Press, 1980, 685 pp.

[29] O. Gérard, O. Jaoul, Oxygen diffusion in San Carlos olivine, J. Geophys. Res. 94 (1989) 4119–4128.

[30] D. Yamazaki, T. Kato, H. Yurimoto, E. Ohtani, M. Toriumi, Silicon self-diffusion in $MgSiO_3$ perovskite at 25 GPa, Phys. Earth Planet. Inter. 119 (2000) 299–309.

[31] R.H. Maddock, Melt origin of fault-generated pseudo-

tachylites demonstrated by textures, Geology 11 (1983) 105–108.

[32] F. Langenhorst, Optische Eigenschaften von experimentell geschockten, kristallinen Feldspäten in Abhängigkeit vom Stoßwellendruck, Diplomarbeit, Institut für Planetologie, WWU Münster, 1989, 105 pp.

[33] E. Ohtani, N. Kagawa, K. Fujino, Stability of majorite (Mg, Fe)SiO$_3$ at high pressures and 1800°C, Earth Planet. Sci. Lett. 102 (1991) 158–166.

[34] N. Funamori, T. Yagi, N. Miyajima, K. Fujino, Transformation in garnet from orthorhombic perovskite to LiNbO$_3$ phase on release of pressure, Science 275 (1997) 513–515.

[35] F. Guyot, M. Madon, J. Peyronneau, J.P. Poirier, X-ray microanalysis of high-pressure/high-temperature phases synthesized from natural olivine in a diamond anvil cell, Earth Planet. Sci. Lett. 90 (1988) 52–64.